

Article

Optical and Spectroscopic Properties of Ho:Lu₂O₃ Transparent Ceramics Elaborated by Spark Plasma Sintering

Lucas Viers¹, Simon Guené-Girard² , Gilles Dalla-Barba³, Véronique Jubéra² , Éric Cormier³, Rémy Boulesteix^{1,*}  and Alexandre Maître¹ 

¹ Faculty of Science and Technology, University of Limoges, CNRS, IRCER, UMR 7315, F-87068 Limoges, France

² Bordeaux INP, University of Bordeaux, CNRS, ICMCB, UMR 5026, F-33600 Pessac, France

³ Institut d'Optique Graduate School, University of Bordeaux, CNRS, LP2N, UMR 5298, F-33400 Talence, France

* Correspondence: remy.boulesteix@unilim.fr

Abstract: In this work, transparent ceramics were manufactured from nanopowders synthesized by aqueous coprecipitation followed by Spark Plasma Sintering (SPS) to ensure rapid and full densification. The photoluminescence of Ho:Lu₂O₃ transparent ceramics was studied in the Visible and IR domains as a function of Ho³⁺ dopant level from 0.5 at.% to 10 at.%. A cross-relaxation mechanism was identified and favors the 2 μm emission. All of the obtained results indicate that the optical properties are very similar between Lu_{2-x}Ho_xO₃ transparent ceramics and single crystals. Thus, the SPS technique appears to be a very promising method to manufacture such ceramics, which could be used as amplifier media for high-energy solid-state lasers.

Keywords: Lu₂O₃; holmium; transparent ceramics; photoluminescence; lifetime; SPS



Citation: Viers, L.; Guené-Girard, S.; Dalla-Barba, G.; Jubéra, V.; Cormier, É.; Boulesteix, R.; Maître, A. Optical and Spectroscopic Properties of Ho:Lu₂O₃ Transparent Ceramics Elaborated by Spark Plasma Sintering. *Ceramics* **2024**, *7*, 208–221. <https://doi.org/10.3390/ceramics7010013>

Academic Editor: Yiquan Wu

Received: 9 December 2023

Revised: 31 January 2024

Accepted: 6 February 2024

Published: 8 February 2024



Copyright: © 2024 by the authors. Licensee MDPI, Basel, Switzerland. This article is an open access article distributed under the terms and conditions of the Creative Commons Attribution (CC BY) license (<https://creativecommons.org/licenses/by/4.0/>).

1. Introduction

In recent years, transparent ceramics have appeared as a very interesting new class of material for high-power solid-state lasers, leading to the development of multi-kilowatt laser systems [1–4]. Among the variety of the targeted laser characteristics, lasers emitting at 2 μm have been mainly studied for their great potential in the medical field because of the absorption bands of water around this wavelength [5–8]. Compared to other 2 μm emitting ions, Ho³⁺ has the advantage of presenting the largest emission cross-section [9]. Due to their high mechanical resistance, good chemical stability and high thermal conductivity, rare-earth sesquioxides (Sc₂O₃, Y₂O₃ and Lu₂O₃) and garnet structures like YAG (Yttrium Aluminum Garnet) are well adapted and the most used host matrix for such ions [10–13]. Among these materials, Lu₂O₃ is of primary interest because it maintains a high thermal conductivity close to 12 W·m⁻¹·K⁻¹ even for high concentrations of dopant [14].

A high concentration of active ion has great potential for use in high-power laser applications, especially in sesquioxide ceramic matrices where the dopant is inserted in a solid solution [15,16]. Indeed, it can be supposed that a higher doping rate could induce a higher luminescence intensity [17,18]. However, a high dopant volume density can also generate undesired energy transfers, called non-radiative transitions, such as cross-relaxation (CR) or excited-state absorption (ESA), causing quenching of the photoluminescence signal. For the Ho³⁺ ion, the most common transfers are CRs between two ions, called the donor and acceptor, which are performed by up-conversion or down-conversion depending on the initial state of the acceptor and the final state of the donor [19].

The main results concerning the previous developments of sesquioxide ceramics for laser applications were recently summarized in the review of Liu et al. [20]. According to their conclusions, Lu₂O₃ sesquioxide ceramics seem to be the most promising host materials for high-power laser operation. However, they highlight the long road ahead to obtain transparent sesquioxide ceramics of large size and high optical quality. Especially, they pointed out the crucial role played by the synthesis step of nanopowders, as well as

the production of powder compacts with ideal microstructures. According to the works cited in the literature, the elaboration of transparent ceramics requires control of each process step, especially that of sintering. In fact, full densification and total elimination of porosity is mandatory to ensure high optical properties and high laser performances. Pressureless sintering under vacuum, pressure-assisted densification or a combination of these techniques is an efficient way to remove all pores, and non-conventional sintering techniques like Hot Pressing (HP), Hot Isostatic Pressing (HIP) or Spark Plasma Sintering (SPS) also called Field Assisted Sintering Technique—FAST) have been developed and extensively studied for a wide variety of ceramics. Some recent studies were lead, for example, on Y_2O_3 by HP + HIP [21], $Yb:Lu_2O_3$ and $Tm:Lu_2O_3$ by vacuum sintering + HIP [22,23] or $Er:(Sc_xY_{1-x})_2O_3$ by vacuum sintering [24]. Among other techniques, Spark Plasma Sintering relies on the densification of a powder inside an electrically conductive matrix, heated by the Joule effect thanks to the application of a pulsed current with a high intensity, and submitted to a uniaxial pressure generally in the range of 50–150 MPa. SPS is increasingly used for fast and efficient densification of numerous ceramics, including nitrides, carbides and oxides [25]. However, the fast shrinkage and physical phenomena involved during sintering lead to a lack of knowledge on sintering mechanisms, more precisely on the densification step and the subsequently formed microstructures. Moreover, carbon contamination from the common use of a graphite matrix is a main issue often encountered for the sintering of oxides and could strongly affect their optical and spectroscopic properties [26]. Concerning the elaboration of transparent ceramics, few studies have compared the microstructure optical properties' relationships to other non-conventional sintering techniques or have highlighted the specificities of SPS on this family of materials. As an example, some studies were interested in $Nd:Lu_2O_3$ [27,28] or $Yb:Sc_2O_3$ [29] ceramics elaborated by either SPS or HIP techniques. Their main conclusions highlighted that such ceramics in the rare-earth oxide family have similar optical properties to single crystals. In the case of the Ho^{3+} ion, no study has been reported on the implication of the fabrication process parameters on the luminescence properties of as-obtained materials, more especially on the CR mechanisms.

In this work, transparent ceramics of Lu_2O_3 with various Ho^{3+} doping rates were manufactured by a process combining nanopowder synthesis and direct densification by Spark Plasma Sintering. Chemical synthesis by the co-precipitation route has the advantage of producing well-crystallized Ho-doped Lu_2O_3 nanopowders with nanometric grain size and great chemical homogeneity [30]. The microstructure (i.e., grain size), luminescence properties and optical transparency of as-obtained transparent ceramics were studied as a function of the holmium doping content. The results were compared to ones reported in the literature for similar single crystals or transparent ceramics manufactured by HIP in order to highlight the specificities induced by the SPS process.

2. Materials and Methods

2.1. Synthesis of Ho:Lu₂O₃ Nanopowders

Ho-doped Lu_2O_3 nanopowders were synthesized by inverse co-precipitation. Rare-earth nitrates were used as precursor and ammonium bicarbonate as precipitant. Commercial oxides of Lu_2O_3 and Ho_2O_3 (AUER REMY, Lehvoss group, Hamburg, Germany) were first dissolved in hot nitric acid (HNO_3 , 65 vol.%, Thermo Fisher Scientific, Waltham, MA, USA). The nitrate solution was poured drop by drop at a rate of $3\text{ mL}\cdot\text{min}^{-1}$ into the solution of ammonium bicarbonate (NH_4HCO_3 , 99wt.%, Acros Organics, Thermo Fisher Scientific, Waltham, MA, USA). The co-precipitation was operated at room temperature with vortex stirring according to the set-up described in Figure 1.

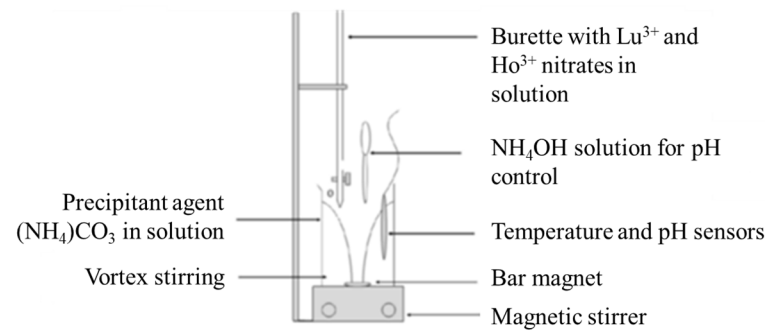


Figure 1. Set-up used for Ho:Lu₂O₃ precipitation.

Ammonia solution (NH₄OH, 35 vol.%, Thermo Fisher Scientific, Waltham, MA, USA) was added to maintain the pH at 9. Then, the solution was aged for 24 h under stirring at room temperature. The obtained precipitate was washed three times with distilled water by centrifugation and three times with ethanol and was dried at 70 °C. The dried precipitate was milled in an agate mortar and calcined at 1000 °C for 2 h under air to form the final crystallized Ho:Lu₂O₃ nanopowder. Powder morphology, structure and chemical homogeneity were obtained by TEM (Transmission Electronic Microscopy) in classical or scanning (STEM) modes and high-resolution TEM coupled with SAED (Selected Area Electron Diffraction) (2100 F, JEOL, Tokyo, Japan). Crystalline phases were identified by X-ray diffraction analyses (D8, Bruker, Karlsruhe, Germany) using CuK α radiation. CuK α 2 radiation contribution was removed and obtained diagrams were indexed with DIFFRACplus EVATM software V5 and the PDFmainTM database.

The TEM observations reported in Figure 2a show a slightly edged shape and narrow size distribution of particles with a mean diameter of about 63 nm. No holmium segregation in the form of isolated Ho₂O₃ particles was detected, as illustrated by the STEM micrograph in Figure 2b. That means there is no differential precipitation of Ho and Lu cations during the synthesis process. The particles also appeared well crystallized in the bixbyite structure (Ia-3, cubic C-type), as revealed by diffraction pattern (Figure 2c). As a result, the Ho:Lu₂O₃ nanopowder can be considered as a Lu_(2-x)Ho_xO₃ homogeneous solid-solution ($x = 0.02$ for 1 at.% holmium doping content) with a cubic crystalline structure. The diffraction patterns registered as a function of the calcination temperature in Figure 2d also prove that the powder is single phased in the bixbyite structure and well crystallized for temperatures higher than 600 °C. A calcination temperature of 1000 °C was chosen regarding the higher crystallinity of the powder particles at this temperature.

2.2. Densification by Spark Plasma Sintering

A commercial device (825 series 8000 A, FUJI-SPS, Saitama, Japan) was used for SPS experiments. The powder samples were put in a 13 mm diameter graphite die with Papyex[®] foil (MERSEN, La Défense, France). Sintering experiments were led under primary vacuum ($P < 20$ Pa) with a pulse sequence of 12:2. A digital IR pyrometer was used for thermal regulation on the surface of the graphite die, which started detecting at a minimum temperature of 573 °C. For all treatments used to elaborate fully dense ceramics, the heating rate was fixed to 100 °C·min⁻¹ until 1200 °C. Then, the heating rate was 10 °C·min⁻¹ until 1400 °C, where the temperature was maintained for 15 min under uniaxial pressure of 130 MPa. The cooling rate was 100 °C·min⁻¹. Then, ceramics were annealed under air at 985 °C for at least 50 h to re-oxidize them and eliminate the carbon contamination caused by the contact with graphite.

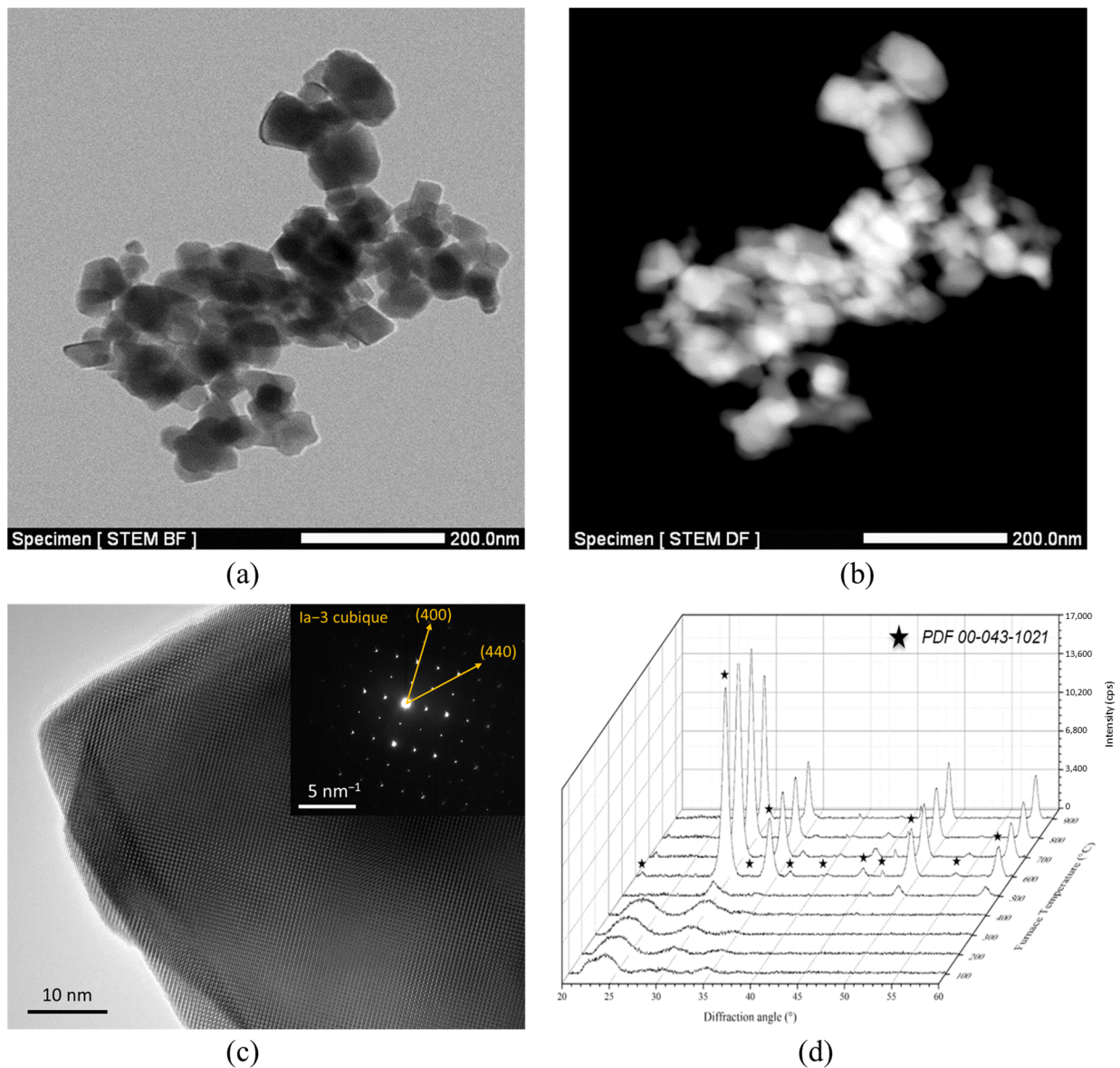


Figure 2. STEM micrographs of the coprecipitated 1 at.%Ho:Lu₂O₃ powder calcined at 1000 °C in bright field (a) or in dark field (b), and high-resolution TEM micrograph with corresponding diffraction pattern (c). XRD patterns registered as a function of the calcination temperature of 1 at.%Ho:Lu₂O₃ powder (d).

2.3. Characterization of Sintered Samples

Prior to optical characterizations, the samples were ground to obtain flat and parallel surfaces and then mirror polished with 30 nm colloidal silica after pre-polishing with SiC papers and diamond pastes. A Cary 5000 spectrophotometer was used to record the transmission curves of transparent samples (Agilent, Santa Clara, CA, USA). The spectra resolution was 1 nm with an integration time equal to 0.1 s.

The photoluminescence spectra of various doped ceramics were obtained from 450 nm to 2200 nm into 3 sub-intervals: Visible [450–800 nm], Near-IR [1000–1300 nm] and Mid-IR [1800–2200 nm]. For all ranges, a photoluminescence spectrometer was used (Fluorolog3, Horiba, Kyoto, Japan) using a 450 W Xe lamp for excitation in Visible and 450 nm laser diode (50 mW) for Near-IR and Mid-IR. For detection, a photo multiplier detector (PMT-Hamamatsu R298, Shizuoka, Japan) was used in Visible, an InGaAs detector for Near-IR and a PbS photoconductor for Mid-IR. For Visible acquisitions, the spectral resolution was 2 nm/mm of opening slits (for both entry and exit ones). Some corrections were applied

to the raw spectra to account for variations in the intensity of the excitation source, set-up geometry and detector sensitivity. For measurements in IR range, the spectral resolution was 12 nm/mm of opening slits and the integration time was 0.5 s.

Lifetime measurements were performed with a 10 nm step-by for each wavelength using an Optical Parametric Oscillator (OPO) for source pumping. Infrared lifetime measurements were performed with an Edinburgh FLS1000 spectrometer coupled with a digital Tektronix oscilloscope to record the time-dependent decay. All the measurements were taken at room temperature.

3. Results

3.1. Sample Microstructure and Optical Transmittance

After sintering at 1400 °C for 15 min, annealing and polishing, Lu₂O₃ ceramics with doping rates from 0.5 at.% to 10 at.% Ho were obtained (Figure 3). All specimens were 2 mm thick and presented good transparency.



Figure 3. Transparent Ho:Lu₂O₃ ceramics with various Ho³⁺ doping rates (from the left to the right: 0.5 at.%, 1 at.%, 5 at.% and 10 at.%) sintered by SPS at 1400 °C for 15 min under 130 MPa of uniaxial pressure.

The SEM micrographs taken for the 1 at.%Ho:Lu₂O₃ sample (Figure 4a) showed a dense microstructure with a small and homogeneous grain size in the order of 200–500 nm. Nevertheless, few intergranular and/or intragranular residual pores were also found, especially by the TEM observations (Figure 4b). Their diameter did not exceed 50 nm and their concentration was estimated to be 90 pores·μm⁻³. These defects could be related to the presence of microstructural inhomogeneities in powder compacts before sintering and/or rapid grain growth [31]. In fact, it has been highlighted in a previous paper that grain growth starts to be significant for temperatures higher than 1300 °C in such ceramics during sintering by SPS, independently of the applied pressure [32].

The transmission curves of the samples are presented on Figure 5. Data have been obtained for wavelengths from 400 nm to 2500 nm. All of the ceramics present the same optical absorption peaks corresponding to 4f electronic transitions of Ho³⁺ ion with corresponding intensity generally increasing with the doping rate. The most intense absorption peaks between 1800 nm and 2200 nm correspond to the ⁵I₈→⁵I₇ transition level. The optical transmittance baseline of all samples presents a continuous decrease from wavelengths of 1200 nm to 300 nm. The obtained curves were compared to the maximum theoretical transmittance of the Lu₂O₃ samples. To determine these values, one has to consider the general law giving the transmittance of a transparent material (Equation (1)):

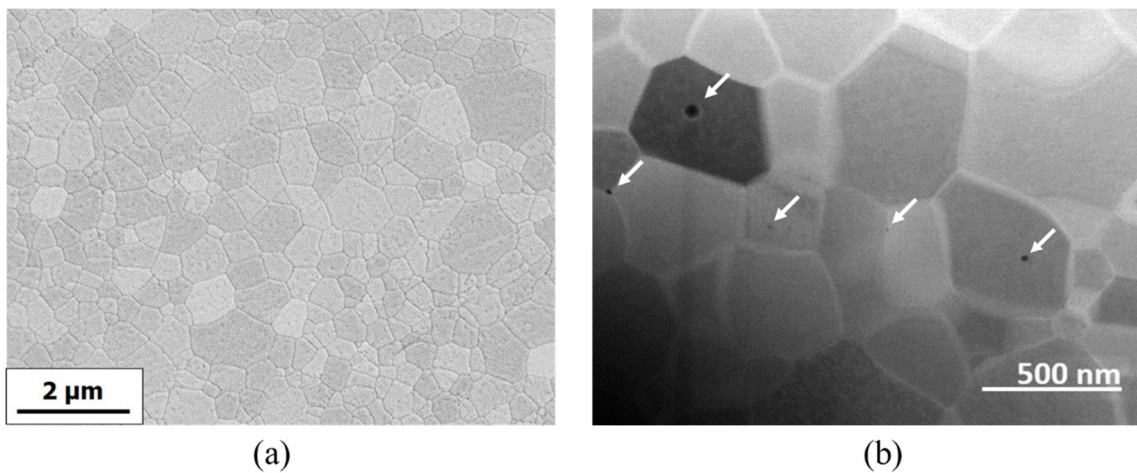


Figure 4. SEM (a) and TEM (b) micrographs of transparent 1 at.%Ho:Lu₂O₃ ceramics sintered by SPS at 1400 °C for 15 min under 130 MPa of uniaxial pressure. Residual porosity was identified by TEM (white arrows).

$$T(\lambda) = T_{max} \exp(-\alpha x) \tag{1}$$

where T_{max} is the maximal transmittance that could be obtained for a perfectly polished sample with planar and parallel surfaces, α is the attenuation coefficient and x is the sample thickness. By considering multiple reflections at the sample’s surface (no antireflective coatings were applied in our case), the maximal transmittance at normal incidence is given by Equation (2):

$$T_{max}(\lambda) = \frac{2n(\lambda)}{(1 + n(\lambda)^2)} \tag{2}$$

where $n(\lambda)$ is the refractive index of cubic Lu₂O₃ given by Equation (3) [33]:

$$n(\lambda)^2 = 3.6196 + \frac{0.04131}{\lambda^2 - 0.0238} - 0.00856 \cdot \lambda^2 \tag{3}$$

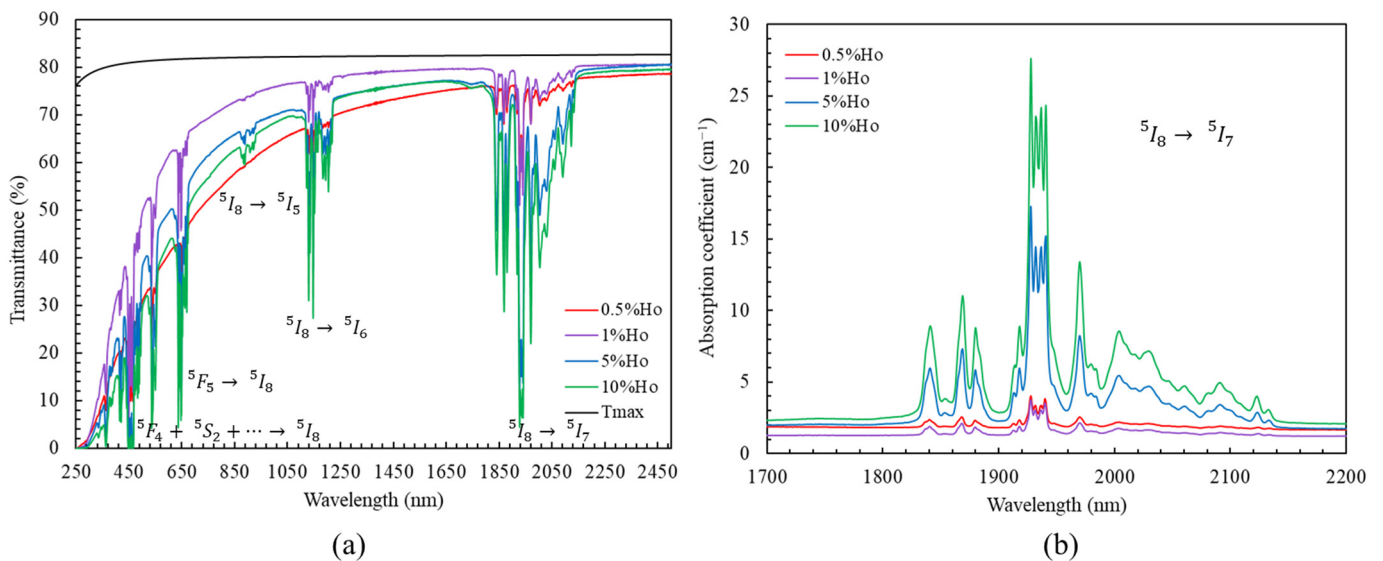


Figure 5. Optical transmission (a) and absorption (b) as a function of wavelength of Ho:Lu₂O₃ transparent ceramics with various Ho³⁺ doping rates.

As a result, one is able to calculate the maximum transmittance value for a perfectly transparent Lu_2O_3 sample. The values are reported in Figure 5.

According to Figure 5a, a strong difference appears between the maximum transmittance and the transmittance baseline of Lu_2O_3 samples. This phenomenon is well-known for transparent ceramics and is generally induced by light scattering coming from residual porosity [34]. However, despite the presence of such optical losses, all Ho-doped Lu_2O_3 ceramics have a transmittance higher than 75%, i.e., more than 90% of the theoretical limit, for wavelengths $> 2 \mu\text{m}$. On the absorption curves (Figure 5b), the effect of the doping rate is clearly highlighted. Indeed, the intensity of absorption transition $^5I_8 \rightarrow ^5I_7$ increases gradually with the Ho^{3+} concentration.

The absorption cross-sections of the Ho: Lu_2O_3 ceramics σ_{abs} were then calculated for all dopant contents from linear absorption coefficient α_λ and by using Equations (4) and (5):

$$\alpha_\lambda = (A_\lambda/x) \cdot \ln(10) \quad (4)$$

$$\sigma_{\text{abs}} = \alpha_\lambda / C_{\text{Ho}} \quad (5)$$

where A_λ is the absorbance for a specific wavelength λ , x is the thickness of sample and C_{Ho} is the volume density of Ho^{3+} . The values of volumetric density of Ho^{3+} (Table 1) were determined thanks to Equation (3) below:

$$C_{\text{Ho}} = (\rho \cdot \% \text{at}_{\text{Ho}} \cdot N_A) / (M_{\text{Lu}_2\text{O}_3:\text{Ho}}) \quad (6)$$

where ρ is the theoretical volumetric mass of Lu_2O_3 with Ia-3 cubic crystalline structure (obtained by XRD measurements), $\% \text{at}_{\text{Ho}}$ is the doping rate, N_A is the Avogadro constant and $M_{\text{Lu}_2\text{O}_3:\text{Ho}}$ is the molar mass of $\text{Lu}_{2-x}\text{Ho}_x\text{O}_3$ compound at a specific doping rate ($0.01 < x < 0.2$).

Table 1. Spectroscopic characteristics of $\text{Lu}_{2-x}\text{Ho}_x\text{O}_3$ samples as a function of Ho^{3+} concentration.

| %at. Ho | 0.5% | 1% | 5% | 10% |
|-------------------------------------------------------|------------------------|------------------------|------------------------|------------------------|
| C_{Ho} (cm^{-3}) | 1.43×10^{20} | 2.85×10^{20} | 1.42×10^{21} | 2.84×10^{21} |
| Absorption cross section at 1927 nm (cm^2) | 1.26×10^{-20} | 1.03×10^{-20} | 1.26×10^{-20} | 1.03×10^{-20} |
| Fluorescence lifetime at 2030 nm (ms) | - | 11.5 | - | 4.92 |

The data reported in Table 1 were used to plot the evolution of the absorption cross-section in the wavelength range 1900–1960 nm for all samples (Figure 6). It was shown that the curves seemed to follow the same evolution of σ_{abs} whatever the doping rate. Moreover, they overlapped despite a slight offset for 0.5% and 5%, which was obviously caused by a lower transmittance baseline (i.e., higher scattering by residual porosity) obtained for both samples. However, for the samples with low residual scattering, the calculated value of σ_{abs} was approximately $1 \times 10^{-20} \text{ cm}^2$ at 1927 nm, which corresponded to the measured data for some Ho-doped systems, for example Ho:YAG [35].

3.2. Photoluminescence and Fluorescence Decay Time

To highlight the different energy transfers and associated light emissions and to attempt to locate some specificities of the elaboration process by SPS, photoluminescence spectroscopy was carried out on all samples in three interesting wavelength domains to highlight potential CR transitions: Visible (from 450 to 800 nm), Near-IR (from 1000 to 1300 nm) and Mid-IR (from 1800 to 2200 nm). The as-obtained results are summarized in Figure 7.

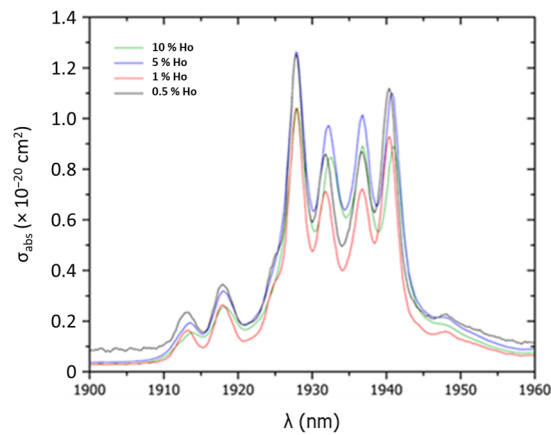


Figure 6. Evolution of absorption cross-section of Ho:Lu₂O₃ transparent ceramics with various Ho³⁺ doping rates.

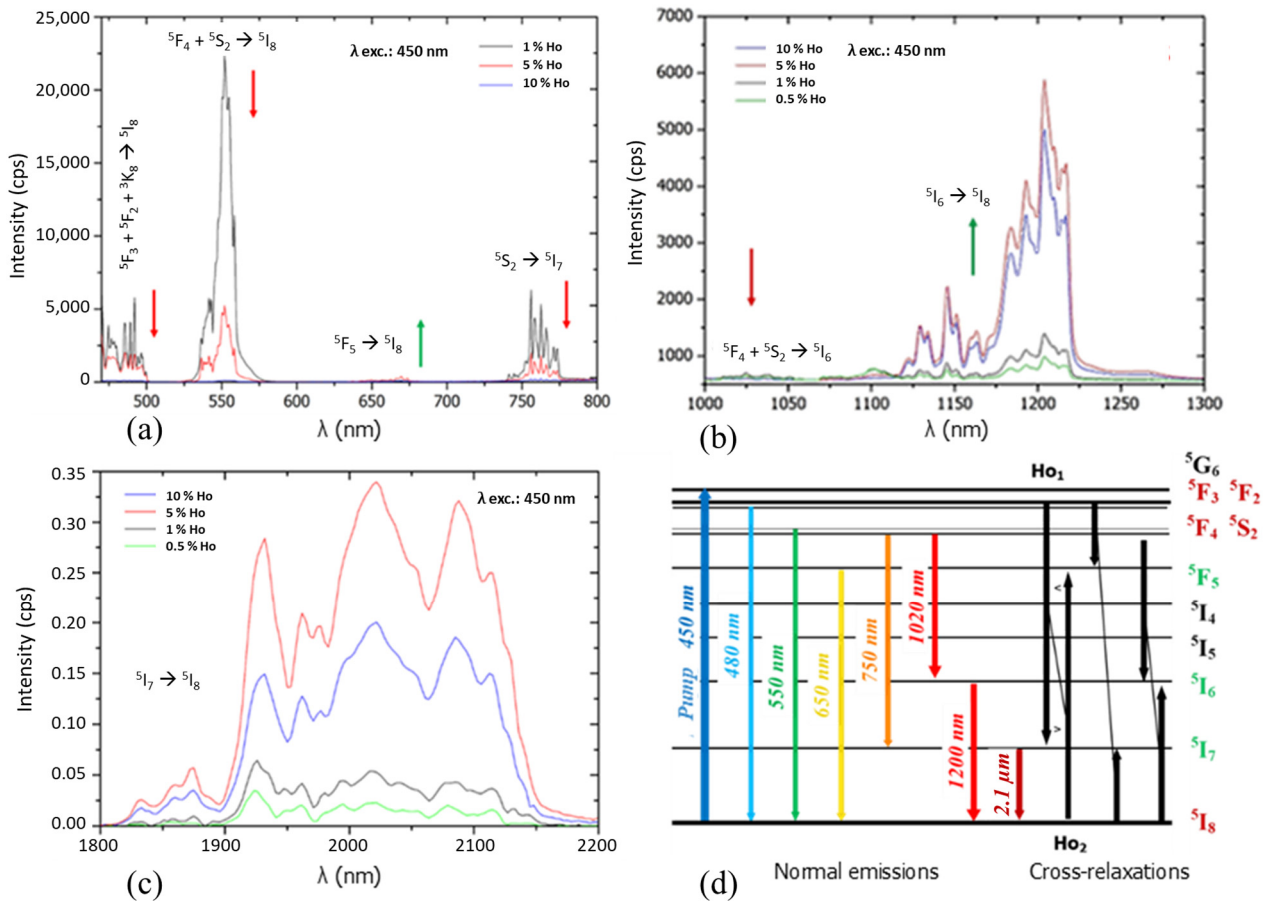


Figure 7. Emission spectra (excitation at 450 nm) of Ho:Lu₂O₃ transparent ceramics in the Visible range (a), Near-IR range (b) and Mid-IR (c) and the associated energy levels diagram built from experimentation (d).

In the Visible range, the emission bands symbolized by red arrows presented a strong decrease when the doping rate increased, with an extinction at 10 at.%Ho (Figure 7a). The identified transitions were $^5F_3 + ^5F_2 + ^3K_8 \rightarrow ^5I_8$ at 480 nm, $^5F_4 + ^5S_2 \rightarrow ^5I_8$ at 550 nm and $^5S_2 \rightarrow ^5I_7$ at 750 nm. However, the transition at 650 nm corresponding to $^5F_5 \rightarrow ^5I_8$ was the only one to increase when the Ho³⁺ content increased. This change in the relative lines intensity was also observed in the Near-IR range, where the transition $^5F_4 + ^5S_2 \rightarrow ^5I_6$ at 1020 nm decreased, whereas the one at 1200 nm, associated with $^5I_6 \rightarrow ^5I_8$, increased

until Holmium doping reached 5%. A maximum of the ${}^5I_7 \rightarrow {}^5I_8$ transition in Mid-IR at 1.8–2.1 μm was observed for the same Ho^{3+} content (Figure 7b,c).

These variations in the intensities of the emission bands are generally representative of non-radiative transitions occurring in the system when the doping rate increases [19,36]. Indeed, when the dopant volume density increases, the average distance between the two Ho^{3+} ions is smaller, which facilitates undesired interactions and the generation of a concentration quenching phenomenon. In addition to this loss of emission intensity due to energy transfer on defects, it is also possible to observe some possible mechanisms corresponding to Cross-Relaxation (CR) energy transfers described in Figure 7d [37], depending on the Ho^{3+} content:

- (1) At a low doping rate (<1%), and after excitation according to the 450 nm transition ${}^5I_8 \rightarrow {}^5G_6$, a cascade of transitions occurs. First, ${}^5F_3 + {}^5F_2 + {}^3K_8 \rightarrow {}^5I_8$ radiative transition at 480 nm happens, as well as a non-radiative ${}^5G_6 \rightarrow {}^5F_4 + {}^5S_2$ transition. From this electronic level, two optical emissions occur at 550 nm and 750 nm corresponding, respectively, to the ${}^5F_4 + {}^5S_2 \rightarrow {}^5I_8$ and ${}^5F_4 + {}^5S_2 \rightarrow {}^5I_7$ transitions. In a second step, the transition ${}^5I_7 \rightarrow {}^5I_8$ at 2100 nm occurs. From level ${}^5F_4, {}^5S_2$, a second transition ${}^5F_4 + {}^5S_2 \rightarrow {}^5I_6$ at 1020 nm, as well as a non-radiative transition ${}^5F_4 + {}^5S_2 \rightarrow {}^5F_5$, is observed. Then, from the 5F_5 electronic level, an emission is present at 650 nm, linked to the ${}^5F_5 \rightarrow {}^5I_8$ transition.
- (2) When the doping increases, due to the increase in the volume concentration of Ho^{3+} ions in the matrix, $\text{Ho}_1\text{-Ho}_2$ non-radiative Cross-Relaxation interactions are increasingly favored. These interactions, which induce modification of electronic level populations, lead to the overcrowding of the 5I_7 and 5F_5 levels according to the ${}^5I_8 \rightarrow {}^5I_7$ or ${}^5F_3 + {}^5F_2 \rightarrow {}^5I_7$ transitions of Ho_1 and ${}^5F_3 + {}^5F_2 \rightarrow {}^5F_5$ or ${}^5I_8 \rightarrow {}^5F_5$ of Ho_2 . Thus, the intensity of the ${}^5I_7 \rightarrow {}^5I_8$ transition in the Mid-IR at 2100 nm increases at the expense of Visible transitions up to 5% in Ho^{3+} ions (Figure 7a,c). Finally, a last relaxation takes place and induces the overcrowding of level 5I_6 according to the transitions ${}^5F_4 + {}^5S_2 \rightarrow {}^5I_6$ and ${}^5I_8 \rightarrow {}^5I_6$. Hence, the transition in the Near-IR ${}^5I_6 \rightarrow {}^5I_8$ at 1200 μm is favored (Figure 7b).
- (3) Above 5%, the phenomenon of fluorescence quenching by concentration is observed for all transitions [38]. For the highest concentration tested, namely 10% ($2.84 \times 10^{21} \text{ ions}\cdot\text{cm}^{-3}$), the fluorescence intensity in the Near-IR and Mid-IR is reduced by 40% compared to 5% ($1.42 \times 10^{21} \text{ ions}\cdot\text{cm}^{-3}$) (Figure 8b,c).

Figure 9 shows the fluorescence lifetime measured on the two extreme doping rates (i.e., 1% and 10%) in order to see the influence of Ho^{3+} concentration on the fluorescence decay of ${}^5I_7 \rightarrow {}^5I_8$ laser transition at 2100 nm. Data were obtained for an excitation at 1850 nm and an emission at 2030 nm, corresponding to the maximum intensity observed in Figure 7c. The fluorescence lifetime was obtained by curve fitting with an exponential function. For 1%, a lifetime of 11.5 ms was obtained for 5I_7 level state. Then, this lifetime decreased from 11.5 ms to 4.92 ms when the doping rate increased from 1% to 10%, which is in accordance with the literature on Ho-doped sesquioxides [39].

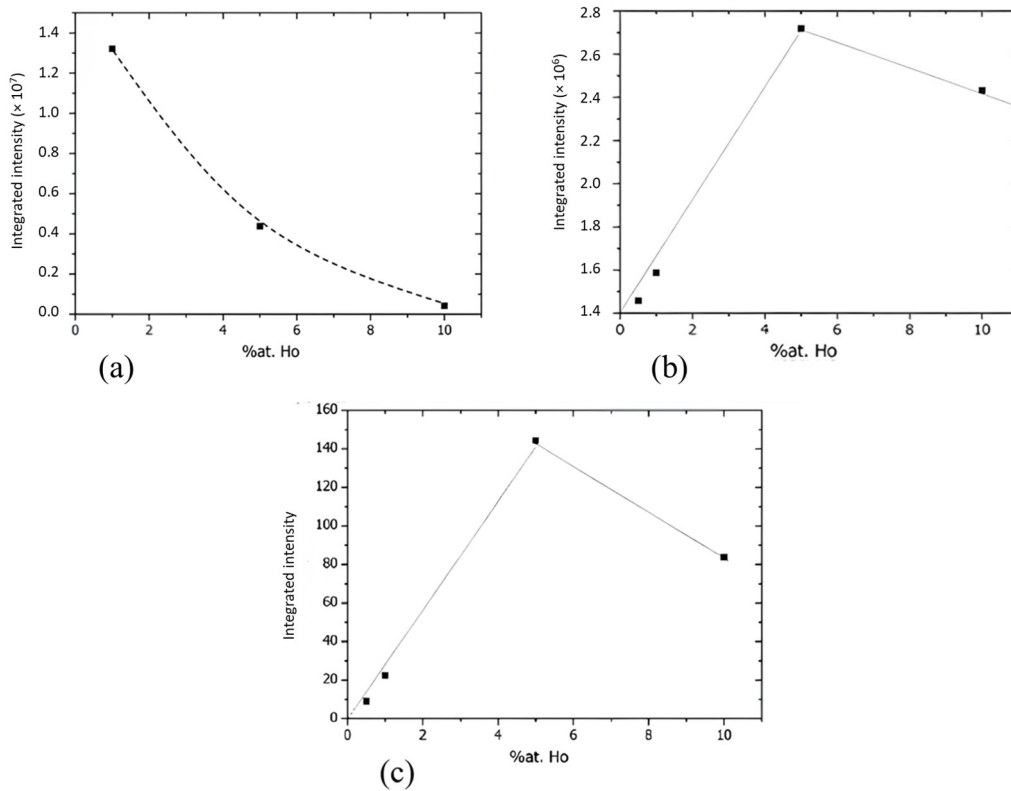


Figure 8. Evolution of integrated emission intensities of Ho:Lu₂O₃ transparent ceramics in the Visible (400–800 nm) range, (a) Near-IR range (1000–1300 nm) (b) and Mid-IR range (1800–2200 nm) (c).

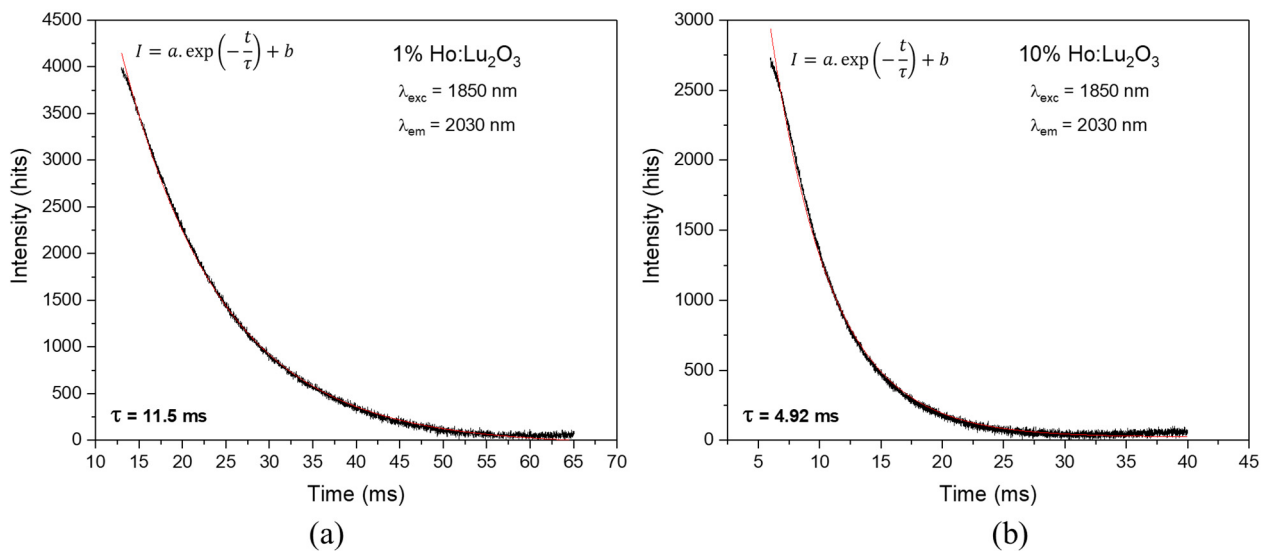


Figure 9. Fluorescence lifetime of 1% (a) and 10% (b) transparent ceramics. Fitted curves are represented in red lines with associated exponential decay function.

This phenomenon confirms the concentration quenching of the 2.1 μ m emission caused by the high active ion density inside material, as mentioned in Section 3.1.

4. Discussion

In this work, transparent Lu_{2-x}Ho_xO₃ ceramics with fine microstructures ($G < 1$ μ m) were obtained thanks to the SPS sintering technique. It increases the list of Lu₂O₃-based transparent ceramics obtained by SPS, previously doped with Nd [27,28], Tm [13] or Yb [40], proving the capability and versatility of this technique. Some of them have proven

sufficient optical quality to observe a laser oscillation. One can cite also the works of Toci et al., who first demonstrated a laser effect with a 1 at.% Nd:Lu₂O₃ transparent ceramic obtained by SPS [41]. A few years later, Xu et al. achieved a laser slope efficiency of 38% with a maximum output of 1.25 W [42]. Many other available sintering techniques have been reported in the literature, such as air, vacuum or hot pressing (HP) pre-sintering followed by high-temperature post-HIP for a long time. The main drawback in this case relies on the large-sized grains ($G > 10 \mu\text{m}$), which are detrimental to the thermal and mechanical properties of ceramics. As an example, Kim et al. obtained HP + HIP Ho³⁺-doped Lu₂O₃ ceramics with an average grain size around 40–50 μm [39]. This difference is a consequence of the thermomechanical cycle used during the SPS treatment, performed at lower maximum temperatures and faster heating rates, which drastically limit grain growth during sintering [32]. As a result, compared to HIP, some differences in the optical properties, originating from the difference in the microstructure or carbon contamination of the samples after SPS treatment, could be expected.

First, concerning the effect of grain size, it seems to have no significant effect for Ho-doped Lu₂O₃. Indeed, by comparing data to 2% Ho-doped Lu₂O₃ ceramic obtained by HIP [39], a similar fluorescence lifetime in the order of 10 ms is obtained at a wavelength of 2140 nm. This value is also of the same order of magnitude as that obtained for single crystals of similar composition. The mean grain diameter obtained in this work is around 50 times lower than that obtained by HIP. That means that the volume of grains is about $(G/G')^3 \sim 10^5$ lower in our samples and the grain boundaries volume fraction is about $(G'/G) \sim 50$ times higher. Therefore, the environment of Ho at grain boundaries should be similar than that observed in the bulk, and very limited Ho segregation is expected to occur in such material. This shows an advantage of this system for laser applications compared to other ones where dopant segregation at grain boundaries is observed, like in rare-earth-doped fluoride ceramics [43].

Second, concerning the use of SPS treatment, it seems to have no observable effect on the photoluminescence properties or lifetime decay according to results reported in Table 2. For example, on a 1%Ho:Lu₂O₃ single crystal, Dong et al. obtained a similar value of 9.8 ms for the same optical transition at a wavelength of 2030 nm [44]. A similar trend was observed for a lower Ho-doping content [45]. In addition, no additional optical transition, which could be associated with the SPS process, was observed in the absorption or luminescence spectra reported in Figures 5 and 7. Moreover, Capobianco et al. obtained a very similar evolution of Visible transition intensities for Ho:Y₂O₃ samples sintered under air [37]. As a result, the Ho:Lu₂O₃ ceramics elaborated in this study present very similar optical properties compared to ceramics sintered by other techniques, as well as those of single crystals. Nanopowder chemical synthesis coupled with SPS sintering technology appears to be a very promising elaboration process to obtain laser ceramics. However, the optical quality should be still improved, i.e., the residual porosity seen in Figure 4 should be totally removed. Also, the samples are directly in contact with the graphite die during sintering and often present a grey/dark color after sintering. This was assigned by many studies to a reduction in the material linked to carbon contamination, and it can be easily removed by a reoxidation treatment under air at a moderate temperature (i.e., 900–1200 °C). Nevertheless, the time required for such a treatment evolves as a function of e^2 , where e is the thickness of samples, because the rate of the reoxidation process is controlled by solid-state diffusion. As a result, a very long time is required for the reoxidation of samples with centimetric thickness, constituting a strong limitation of the efficiency of the whole process. Further investigations will be carried out on these two points to improve the optical quality of the ceramics and the scalability of the process.

Table 2. Spectroscopic characteristics of $\text{Lu}_{2-x}\text{Ho}_x\text{O}_3$ samples as a function of process parameters.

| Reference | Composition | Material | Sintering | G_{mean} (μm) | T% at 2 μm | λ_{abs} (nm) | σ_{abs} (cm^2) | λ_{em} (nm) | σ_{em} (cm^2) | τ_{rad} (ms) |
|----------------------|---------------------------------------|----------------|--------------------------|-------------------------------------|-----------------------|-----------------------------|-----------------------------------------|----------------------------|----------------------------------------|--------------------------|
| This work | 1%Ho:Lu ₂ O ₃ | Ceramic | SPS + air annealing | <1 μm | 80% | 1927 | 1×10^{-20} | 2030 | | 11.5 |
| Kim et al. [39] | 2%Ho:Lu ₂ O ₃ | Ceramic | Post-HIP + air annealing | 50 μm | >80% | 1942 | - | 2140 | - | 10 |
| Dong et al. [44] | 1%Ho:Lu ₂ O ₃ | Single-crystal | - | - | >80% | 1929 | 1.1×10^{-20} | 2027 | 3.3×10^{-21} | 9.5 |
| Koopmann et al. [45] | 0.3%Ho:Lu ₂ O ₃ | Single-crystal | - | - | >80% | 1928 | 1.2×10^{-20} | 2124 | 4.5×10^{-21} | 10 |

5. Conclusions

$\text{Lu}_{2-x}\text{Ho}_x\text{O}_3$ transparent ceramics with a small grain size (<1 μm) were successfully manufactured by Spark Plasma Sintering of homemade nanopowders. The photoluminescence study performed in the Visible and IR domains has given similar results to those obtained for single crystals of similar compositions. Especially, cross-relaxation mechanisms have been identified and favor the 2 μm emission. Moreover, fluorescence lifetime measurements have highlighted concentration quenching, especially for high doping of 10% Ho. All of the obtained results indicate that the optical properties are very similar between $\text{Lu}_{2-x}\text{Ho}_x\text{O}_3$ transparent ceramics and single crystals. Thus, the distribution of Ho^{3+} ions should be similar in both materials, i.e., no clustering of Ho^{3+} ions in ceramics should take place, whatever the process parameters or the doping level. Finally, SPS appears to be a very promising method to produce transparent polycrystalline ceramics of the rare-earth oxide family. Among them, $\text{Lu}_{2-x}\text{Ho}_x\text{O}_3$ ceramics could substitute single crystals of similar composition and are very promising materials for high-energy solid-state lasers.

Author Contributions: Conceptualization, R.B. and L.V.; methodology, R.B. and L.V.; validation, R.B. and A.M.; formal analysis, L.V.; investigation, L.V. and S.G.-G.; data curation, L.V.; writing—original draft preparation, L.V.; writing—review and editing, R.B., V.J., G.D.-B., É.C. and A.M.; supervision, R.B. and A.M.; project administration, R.B.; funding acquisition, R.B. All authors have read and agreed to the published version of the manuscript.

Funding: This research was funded by the Region Nouvelle-Aquitaine (MISTRAL program n° 2017-1R50311 and HICEMIR program n° 2017-1R50311) and was also supported by an institutional grant from the National Research Agency under the investments for the future program with the reference ANR-10-LABX-0074-01 Sigma-LIM.

Institutional Review Board Statement: Not applicable.

Informed Consent Statement: Not applicable.

Data Availability Statement: The data presented in this study are available on request from the corresponding author. The data are not publicly available due to the data are part of an ongoing study.

Acknowledgments: The authors are grateful to Pierre Carles (IRCER, Limoges, France) for the TEM and STEM observations and Victor Anthony Garcia Rivera (COPL, University Laval) for the lifetime measurements performed in the frame of the International Associated Laboratory (LIA) LuMAQ.

Conflicts of Interest: The authors declare no conflicts of interest. The funders had no role in the design of the study; in the collection, analyses or interpretation of data; in the writing of the manuscript or in the decision to publish the results.

References

1. Ikesue, A.; Aung, Y.L. Ceramic laser materials. *Nat. Photon.* **2008**, *2*, 721–727. [[CrossRef](#)]
2. Sanghera, J.; Bayya, S.; Villalobos, G.; Kim, W.; Frantz, J.; Shaw, B.; Sadowski, B.; Miklos, R.; Baker, C.; Hunt, M.; et al. Transparent ceramics for high-energy laser systems. *Opt. Mater.* **2011**, *33*, 511–518. [[CrossRef](#)]
3. Kim, W.; Villalobos, G.; Baker, C.; Frantz, J.; Shaw, B.; Bayya, S.; Bowman, S.; Sadowski, B.; Hunt, M.; Rock, B.; et al. Overview of transparent optical ceramics for high-energy lasers at NRL. *Appl. Opt.* **2015**, *54*, F210–F221. [[CrossRef](#)]

4. Zhu, D.; Chen, Z.-Z.; Song, Y.-J.; Yuan, L.; Lin, Y.-Y.; Zhang, L.-N.; Cui, D.-F.; Bo, Y.; Peng, Q.-J.; Xu, Z.-Y.; et al. High Power (~10 kW) Yb:YAG Ceramic Slab Laser Operating at 1030 nm. *IEEE Photon. Technol. Lett.* **2023**, *35*, 789–792. [[CrossRef](#)]
5. Zhang, W.X.; Zhou, J.; Liu, W.B.; Li, J.; Wang, L.; Jiang, B.X.; Pan, Y.B.; Cheng, X.J.; Xu, J.Q. Fabrication, properties and laser performance of Ho:YAG transparent ceramic. *J. Alloys Compd.* **2010**, *506*, 745–748. [[CrossRef](#)]
6. Zhang, W.X.; Pan, Y.B.; Zhou, J.; Liu, W.B.; Li, J.; Jiang, B.X.; Cheng, X.J.; Xu, J.Q. Diode-Pumped Tm:YAG Ceramic Laser. *J. Am. Ceram. Soc.* **2009**, *92*, 2434–2437. [[CrossRef](#)]
7. Scholle, K.; Lamrini, S.; Koopmann, P.; Fuhrberg, P. 2 μm Laser Sources and Their Possible Applications. In *Frontiers in Guided Wave Optics and Optoelectronics*; Pal, B., Ed.; IntechOpen: London, UK, 2010.
8. Yang, H.; Zhang, J.; Qin, X.P.; Luo, D.W.; Ma, J.; Tang, D.Y.; Zhang, Q.T. Fabrication and Properties of High Quality Transparent Ho:YAG Ceramics. *Solid State Phenom.* **2012**, *185*, 51–54. [[CrossRef](#)]
9. Payne, S.A.; Chase, L.L.; Smith, L.K.; Kway, W.L.; Krupke, W.F. Infrared cross section measurements for crystals doped with Er^{3+} , Tm^{3+} , and Ho^{3+} . *IEEE J. Quantum Electron.* **1992**, *28*, 2619–2630. [[CrossRef](#)]
10. Wang, Y.; Lan, R.; Mateos, X.; Li, J.; Hu, C.; Li, C.; Suomalainen, S.; Härkönen, A.; Guina, M.; Petrov, V.; et al. Broadly tunable mode-locked Ho:YAG ceramic laser around 21 μm . *Opt. Express* **2016**, *24*, 18003–18012. [[CrossRef](#)] [[PubMed](#)]
11. Chen, H.; Shen, D.; Zhang, J.; Yang, H.; Tang, D.; Zhao, T.; Yang, X. In-band pumped highly efficient Ho:YAG ceramic laser with 21 W output power at 2097 nm. *Opt. Lett.* **2011**, *36*, 1575–1577. [[CrossRef](#)]
12. Cheng, X.; Xu, J.; Wang, M.; Jiang, B.; Zhang, W.; Pan, Y. Ho:YAG ceramic laser pumped by Tm:YLF lasers at room temperature. *Laser Phys. Lett.* **2010**, *7*, 351–354. [[CrossRef](#)]
13. Antipov, O.L.; Novikov, A.A.; Zakharov, N.G.; Zinoviev, A.P. Optical properties and efficient laser oscillation at 2066 nm of novel Tm:Lu₂O₃ ceramics. *Opt. Mater. Express* **2012**, *2*, 183–189. [[CrossRef](#)]
14. Ikesue, A.; Aung, Y.L.; Lupei, V. *Ceramic Lasers*; Cambridge University Press: Cambridge, UK, 2013; p. 165.
15. Salek, G.; Devoti, A.; Garcia, A.; Gaudon, M.; Jubera, V.; Demourgues, A. Tuning the composition of rare earth sesquioxides Gd_{2-x}La_xO₃:Eu³⁺ to control phase transitions at a high temperature to design new highly sensitive luminescence-based thermal sensors. *R. Soc. Chem.* **2016**, *6*, 298–306. [[CrossRef](#)]
16. Permin, D.; Kurashkin, S.; Novikova, A.; Savikin, A.; Gavrishchuk, E.; Balabanov, S.; Khamaletdinova, N. Synthesis and luminescence properties of Yb-doped Y₂O₃, Sc₂O₃ and Lu₂O₃ solid solutions nanopowders. *Opt. Mater.* **2018**, *77*, 240–245. [[CrossRef](#)]
17. Tang, F.; Huang, J.; Guo, W.; Wang, W.; Fei, B.; Cao, Y. Photoluminescence and laser behavior of Yb:YAG ceramic. *Opt. Mater.* **2012**, *34*, 757–760. [[CrossRef](#)]
18. Unal, F.; Kaya, F. Kazmanli, KEffects of dopant rate and calcination parameters on photoluminescence emission of Y₂O₃:Eu³⁺ phosphors: A statistical approach. *Ceram. Int.* **2019**, *45*, 17818–17825. [[CrossRef](#)]
19. Malinowski, M.; Kaczkan, M.; Wnuk, A.; Szuflińska, M. Emission from the high lying excited states of Ho³⁺ ions in YAP and YAG crystals. *J. Lumin.* **2004**, *106*, 269–279. [[CrossRef](#)]
20. Liu, Z.; Ikesue, A.; Li, J. Research progress and prospects of rare-earth doped sesquioxide laser ceramics. *J. Eur. Ceram. Soc.* **2021**, *41*, 3895–3910. [[CrossRef](#)]
21. Fu, Z.; Wu, N.; Long, H.; Hou, Z. Fabrication of fine-grained and high thermal properties Y₂O₃ transparent ceramics without sintering aids. *Opt. Mater.* **2024**, *147*, 114618. [[CrossRef](#)]
22. Liu, Z.; Feng, Y.; Toci, G.; Pirri, A.; Patrizi, B.; Vannini, M.; Li, J. Influence of annealing on microstructures and properties of Yb:Lu₂O₃ transparent ceramics. *J. Am. Ceram. Soc.* **2023**, *107*, 1974–1984. [[CrossRef](#)]
23. Liu, Z.; Toci, G.; Pirri, A.; Patrizi, B.; Feng, Y.; Hu, D.; Chen, H.; Hreniak, D.; Vannini, M.; Li, J. Fabrication and characterizations of Tm:Lu₂O₃ transparent ceramics for 2 μm laser applications. *Opt. Mater.* **2022**, *131*, 112705. [[CrossRef](#)]
24. Maksimov, R.; Shitov, V.; Osipov, V.; Samatov, O.; Vakalov, D.; Malyavin, F.; Basyrova, L.; Loiko, P.; Camy, P. Fabrication, microstructure and mid-infrared luminescence of Er:(Sc_xY_{1-x})₂O₃ transparent ceramics. *Opt. Mater.* **2023**, *137*, 113542. [[CrossRef](#)]
25. Chaim, R.; Levin, M.; Shlayer, A.; Estournes, C. Sintering and densification of nanocrystalline ceramic oxide powders: A review. *Adv. Appl. Ceram.* **2008**, *107*, 159–169. [[CrossRef](#)]
26. Morita, K.; Kim, B.-N.; Yoshida, H.; Hiraga, K.; Sakka, Y. Distribution of carbon contamination in oxide ceramics occurring during spark-plasma-sintering (SPS) processing: II Effect of SPS and loading temperatures. *J. Eur. Ceram. Soc.* **2018**, *38*, 2596–2604. [[CrossRef](#)]
27. Alombert-Goget, G.; Guyot, Y.; Guzik, M.; Boulon, G.; Ito, A.; Goto, T.; Yoshikawa, A.; Kikuchi, M. Nd³⁺-doped Lu₂O₃ transparent sesquioxide ceramics elaborated by the Spark Plasma Sintering (SPS) method. Part 1: Structural, thermal conductivity and spectroscopic characterization. *Opt. Mater.* **2015**, *41*, 3–11. [[CrossRef](#)]
28. Boulesteix, R.; Epherre, R.; Noyau, S.; Vandenhende, M.; Maître, A.; Sallé, C.; Alombert-Goget, G.; Guyot, Y.; Brenier, A. Highly transparent Nd:Lu₂O₃ ceramics obtained by coupling slip-casting and spark plasma sintering. *Scr. Mater.* **2014**, *75*, 54–57. [[CrossRef](#)]
29. Lupei, V.; Lupei, A.; Boulon, G.; Jouini, A.; Ikesue, A. Assessment of the distribution of the Yb³⁺ ions in Sc₂O₃ ceramics from cooperative absorption and emission. *J. Alloys Compd.* **2008**, *451*, 179–181. [[CrossRef](#)]
30. Liu, Z.; Toci, G.; Pirri, A.; Patrizi, B.; Li, J.; Hu, Z.; Wei, J.; Pan, H.; Xie, T.; Vannini, M.; et al. Fabrication and laser operation of Yb:Lu₂O₃ transparent ceramics from co-precipitated nano-powders. *J. Am. Ceram. Soc.* **2019**, *102*, 7491–7499. [[CrossRef](#)]

31. Thoř, T.; Rubeřov, K.; Jakeř, V.; Mikolřov, D.; Cajzl, J.; Havlıcek, J.; Nadherny, L.; Pruřa, F.; Kučerkov, R.; Nikl, M. Dense ceramics of lanthanide-doped Lu₂O₃ prepared by spark plasma sintering. *J. Eur. Ceram. Soc.* **2021**, *41*, 741–751. [[CrossRef](#)]
32. Viers, L.; Delaunay, F.; Boulesteix, R.; Vandenhende, M.; Antou, G.; Matre, A. Study of densification mechanisms during Spark Plasma Sintering of co-precipitated Ho:Lu₂O₃ nanopowders: Application to transparent ceramics for lasers. *J. Eur. Ceram. Soc.* **2021**, *41*, 7199–7207. [[CrossRef](#)]
33. Kaminskii, A.A.; Akchurin, M.S.; Becker, P.; Ueda, K.; Bohaty, L.; Shirakawa, A.; Tokurakawa, M.; Takaichi, K.; Yagi, H.; Dong, J. Mechanical and optical properties of Lu₂O₃ host-ceramics for Ln³⁺ lasants. *Laser Phys. Lett.* **2008**, *5*, 300–303. [[CrossRef](#)]
34. Boulesteix, R.; Matre, A.; Baumard, J.-F.; Rabinovitch, Y.; Reynaud, F. Reynaud, Light scattering by pores in transparent Nd:YAG ceramics for lasers: Correlations between microstructure and optical properties. *Opt. Express* **2010**, *18*, 14992–15002. [[CrossRef](#)]
35. Brown, D.C.; Envid, V.; Zembek, J. Ho:YAG absorption cross sections from 1700 to 2200 nm at 83, 175, and 295 K. *Appl. Opt.* **2012**, *51*, 8147–8158. [[CrossRef](#)]
36. Silver, J.; Barrett, E.; Marsh, P.J.; Withnall, R. Yttrium Oxide Upconverting Phosphors. 5. Upconversion Luminescent Emission from Holmium-Doped Yttrium Oxide under 632.8 nm Light Excitation. *J. Phys. Chem. B* **2003**, *107*, 9236–9242. [[CrossRef](#)]
37. Capobianco, J.A.; Boyer, J.C.; Vetrone, F.; Speghini, A.; Bettinelli, M. Optical Spectroscopy and Upconversion Studies of Ho³⁺-Doped Bulk and Nanocrystalline Y₂O₃. *Chem. Mater.* **2002**, *14*, 2915–2921. [[CrossRef](#)]
38. Auzel, F.; Baldacchini, G.; Laversenne, L.; Boulon, G. Radiation trapping and self-quenching analysis in Yb³⁺, Er³⁺, and Ho³⁺ doped Y₂O₃. *Opt. Mater.* **2003**, *24*, 103–109. [[CrossRef](#)]
39. Kim, W.; Baker, C.; Bowman, S.; Florea, C.; Villalobos, G.; Shaw, B.; Sadowski, B.; Hunt, M.; Aggarwal, I.; Sanghera, J. Laser oscillation from Ho³⁺ doped Lu₂O₃ ceramics. *Opt. Mater. Express* **2013**, *3*, 913–919. [[CrossRef](#)]
40. Kijko, V.; Maksimov, R.N.; Shitov, V.; Demakov, S. Yurovskikh, ASintering of transparent Yb-doped Lu₂O₃ ceramics using nanopowder produced by laser ablation method. *J. Alloys Compd.* **2015**, *643*, 207–211. [[CrossRef](#)]
41. Toci, G.; Vannini, M.; Ciofini, M.; Lapucci, A.; Pirri, A.; Ito, A.; Goto, T.; Yoshikawa, A.; Ikesue, A.; Alombert-Goget, G.; et al. Nd³⁺-doped Lu₂O₃ transparent sesquioxide ceramics elaborated by the Spark Plasma Sintering (SPS) method. Part 2: First laser output results and comparison with Nd³⁺-doped Lu₂O₃ and Nd³⁺-Y₂O₃ ceramics elaborated by a conventional method. *Opt. Mater.* **2014**, *41*, 12–16. [[CrossRef](#)]
42. Xu, C.; Yang, C.; Zhang, H.; Duan, Y.; Zhu, H.; Tang, D.; Huang, H.; Zhang, J. Efficient laser operation based on transparent Nd:Lu₂O₃ ceramic fabricated by Spark Plasma Sintering. *Opt. Express* **2016**, *24*, 20571–20579. [[CrossRef](#)] [[PubMed](#)]
43. Boulon, G.; Epicier, T.; Zhao, W.; Guzik, M.; Pan, Y.; Jiang, B. *Is There Segregation of Rare Earth Ions in Garnet Optical Ceramics?* Bartolo, B.D., Collins, J., Baldassare, D.B., John, C., Eds.; Nano-Optics for enhancing light-matter interactions on a molecular scale. NATO Science for Space and Security Series B: Physics and Biophysics; Springer: Dordrecht, The Netherlands, 2013. [[CrossRef](#)]
44. Dong, J.; Wang, W.; Xue, Y.; Hou, W.; Cao, X.; Xu, X.; Wu, F.; Luo, P.; Wang, Q.; Li, D.; et al. Crystal growth and spectroscopic analysis of Ho:Lu₂O₃ crystal for mid-infrared emission. *J. Lumin.* **2022**, *251*, 119192. [[CrossRef](#)]
45. Koopmann, P.; Lamrini, S.; Scholle, K.; Schafer, M.; Fuhrberg, P.; Huber, G. Multi-watt laser operation and laser parameters of Ho-doped Lu₂O₃ at 2.12 μm. *Opt. Mater. Express* **2011**, *1*, 1447–1456. [[CrossRef](#)]

Disclaimer/Publisher’s Note: The statements, opinions and data contained in all publications are solely those of the individual author(s) and contributor(s) and not of MDPI and/or the editor(s). MDPI and/or the editor(s) disclaim responsibility for any injury to people or property resulting from any ideas, methods, instructions or products referred to in the content.